Whole-Brain High-Resolution Metabolite Mapping with 3D Compressed-Sensing-SENSE-LowRank ^{1}H FID-MRSI

Antoine Klauser[1,2], Paul Klauser[3,4], Frédéric Grouiller[5,6],
Sebastien Courvoisier[1,2], Francois Lazeyras[1,2]

[1] *Department of Radiology and Medical Informatics, University of Geneva, Switzerland*

[2] *Center for Biomedical Imaging (CIBM), Geneva, Switzerland*

[3] *Center for Psychiatric Neuroscience, Department of Psychiatry, Lausanne University Hospital, Switzerland*

[4] *Service for Child and Adolescent Psychiatry, Department of Psychiatry, Lausanne University Hospital, Switzerland*

[5] *Swiss Center for Affective Sciences, University of Geneva, Switzerland and*

[6] *Laboratory of Behavioral Neurology and Imaging of Cognition, Department of Fundamental Neuroscience, University of Geneva, Switzerland*

(Dated: March 26, 2021)

Abstract

There is a growing interest in the neuroscience community to map the distribution of brain metabolites in vivo. Magnetic resonance spectroscopy imaging (MRSI) is often limited by either a poor spatial resolution and/or a long acquisition time which severely limits its applications for clinical or research purposes. Building on a recently developed technique of acquisition-reconstruction for 2D MRSI, we combined fast Cartesian ^{1}H-FID-MRSI acquisition sequence, compressed-sensing acceleration, low-rank total-generalized-variation (TGV) constrained reconstruction in order to realize 3D high-resolution whole-brain MRSI with a significant acquisition time reduction. We first evaluated the acceleration performance using retrospective undersampling of a fully-sampled dataset. Second, a 20 min accelerated MRSI acquistion was performed on the brain of three healthy volunteers resulting in metabolite maps with 5 mm isotropic resolution. The metabolite maps exhibited the detailed neurochemical composition of all brain regions and revealed parts of the underlying brain anatomy. The latter assessment using previous reported knowledge and a brain atlas-based analysis showed the consistency of the concentration contrasts and ratio accross all brain regions. These results acquired on a clinical 3 Tesla MRI demonstrate the successful combination of the 3D ^{1}H-FID-MRSI with a constrained reconstruction to realize the detailed mapping of metabolite concentrations at high-resolution over the whole brain, and with an acquisition time that is compatible with clinical or research settings.

word count = 3805

Keywords

3D magnetic resonance spectroscopic imaging, compressed-sensing, SENSE, Low-Rank, acceleration, whole-brain spectroscopy, brain metabolites, High-field MRI

Data availability statement

The data that support the results of this study are available on request from the corresponding author. The data are not publicly available due to ethical restrictions.

Abbreviations

VOI	volume-of-interest
^{1}H-MRSI	proton magnetic resonance spectroscopic imaging
FID	free induction decay
CS	compressed sensing
CS-SENSE-LR	compressed-sensing sensitivity-encoding low-rank
OVS	outer-volume saturation bands
HSVD	Hankel singular value decomposition
TGV	total generalized variation
SNR	signal to noise ratio
tNAA	N-acetylaspartate + N-acetyl aspartylglutamate
tCre	creatine + phosphocreatine
Cho	choline moiety metabolites
Ins	myo-inositol
Glx	glutamate + glutamine
RMSE	normalized root mean square error
SSIM	structural similarity index
RMS	root mean square
CRLB	Cramer-Rao Lower bound
SSE	spatio-spectral encoding
TR	repetition time
TE	echo time
GM	grey matter
WM	white matter

I. INTRODUCTION

Measurement of the metabolite distributions in three dimensions over the whole human brain using proton magnetic resonance spectroscopic imaging (^{1}H-MRSI) has been the subject of two decades of intense research. From early multi-slice methods [1, 2] covering large portion of the brain to the first development of spatio-spectral encoding (SSE) techniques [3–5] proposed by Mansfield [6], whole brain ^{1}H-MRSI unravels distributions with unique

patterns for each metabolite and provides original physiological information complementary to usual MR imaging. Since then, 3D ^{1}H-MRSI methods for human brain imaging have been improved by implementation of acceleration techniques [7–9] or significant increase in spatial resolution [10, 11]. A complete and exhaustive overview of ^{1}H-MRSI techniques that covers also 2D approaches can be found in review articles [12–14].

Recently, advances in reconstruction methods provided new solutions to the inherent limitations of ^{1}H-MRSI. The ^{1}H-MRSI acquisition geometry is often bounded to a rectangular volume-of-interest (VOI) with saturation of the outer signal to prevent skull lipid contamination. However,recent work on efficient post-acquisition lipid decontamination [15–18] enables measurement of whole brain slices without limited VOI by in plane selective excitation. In addition, employing models including constraints of prior information for ^{1}H-MRSI data reconstruction significantly improves spectral quality and the resulting metabolite distributions [19, 20]. A priori knowledge of the underlying signal can also be exploited for super-resolution [21, 22] or drastic acceleration of ^{1}H-MRSI acquisition [23, 24].

Acquisition of whole-brain MRSI using traditional methods could be particularly lengthy due to the necessity to encode the large 4D k-t space. However, acquisition time can be significantly reduced by several techniques such as the free induction decay (FID)-MRSI acquisition, parallel imaging, and compressed sensing (CS). The FID-MRSI sequence first known for its application in ^{31}P and other nuclei spectroscopic imaging [25, 26], has been more recently proposed for ^{1}H-MRSI [27, 28]. The simple sequence design dramatically shortens acquisition time in comparison with usual spin-echo methods by allowing low-flip-angle excitation and sub-second repetition time (TR). Implementation of parallel imaging techniques in 3D ^{1}H-MRSI of the human brain can reduce the acquisition time by a factor of 2 to 8. [8, 9, 29]. Following the recent developments of CS for MRI [30, 31], the sparsity present in the 3D MRSI signal can also be exploited to accelerate the acquisition of the 4D encoding k-t space. The effectiveness of this approach was demonstrated for ^{13}C or ^{19}F [32, 33] as well as in combination with fast spatial-spectral encoding [34]. The application of CS to ^{1}H-MRSI of the human brain grants accelerations up to a factor of 4 but has been limited to 2D acquisitions so far [17, 35–38].

State-of-the-art techniques offering 3D whole-brain ^{1}H-MRSI often rely on the use of SSE [14] that implies an encoding of the whole 3D space by entire lines. Hence, these approaches allow highly accelerated acquisitions and permit MRSI acquistions of the whole-brain in

high-resolution within an duration compatible with clinical requirements. The trajectory can be either echo-planar [24, 39], concentric circles [10, 40], rosette [41] or spiral [42]. With a signal-to-noise ratio (SNR) / time comparable to Cartesian encoding of same resolution [14], SSE technique might nevertheless results in low SNR data that requires averaging or specific denoising model-based approaches[24]. The method of acceleration presented hereafter relies on undersampling of the Cartesian 3D k-space. Thanks to the non-linear reconstruction process [17], it is anticipated that SNR is preserved or decreases more slowly than linearly with respect to the acceleration. On the other hand, high acceleration is expected to affect the spatial distributions of the MRSI signal as pointed out in previous studies of CS with MRI [43, 44]. In this study, we aim to evaluate the capability of the proposed framework as an alternative to the acceleration of 3D MRSI with SSE.

In this work we present original results of high-resolution 3D ^{1}H-MRSI of the whole human brain on a 3T clinical system. The acquisition-reconstruction scheme combines a fast FID-MRSI high-resolution sequence accelerated by random undersampling and reconstructed with a CS SENSE low-rank model (CS-SENSE-LR [17]) that has been extended to 3D in the present study. This comprehensive approach, combining FID and parallel acquisition schemes to CS-SENSE-LR reconstruction drastically shortens the acquisition time and allows implementation of high-resolution 3D MRSI into clinical and research scanning protocols. As proof of principle, whole-brain 3D metabolite volumes resulting from three healthy volunteers were segmented to assess the specific distribution of metabolites across brain regions and tissue types.High-resolution metabolite mapping will have a great range of applications from neurology to psychiatry [45, 46]. In clinical neuroscience and with usual spectroscopic techniques, interpretation of spectroscopy findings is limited by the VOI approach, neglecting large cerebral parts around the volume selected by the a priori hypothesis. There is a strong need for whole-brain spectroscopy imaging which allows not only the mapping of metabolites in all brain regions but also the integration of brain spectroscopic data with other imaging modalities including structural and diffusion MR [47].

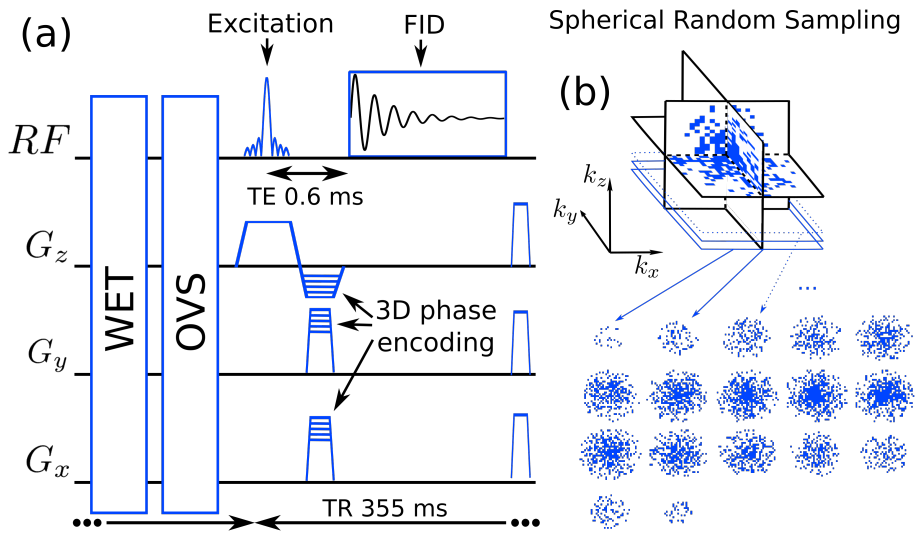

FIG. 1. Schematic of the FID-MRSI sequence with 3D phase encoding (left) preceded by the water suppression enhanced through T1 effects (WET) and outer-volume saturation bands (OVS) sequence blocks. An example of 3D undersampled k-space by factor 3.5 is shown (right)

II. METHODS

A. Sequence and Acquisition

A ^{1}H-FID-MRSI [27, 28] sequence with a 3 dimensional phase encoding was implemented (Fig. 1) on a 3T Prisma fit MRI (Siemens, Erlangen, Germany) using a receiver head coil with $N_c = 64$ elements. A Shinnar-LeRoux optimized slab-selective excitation pulse of 0.9 ms was used with a 9.5-kHz bandwidth. WET [48] water suppression was implemented with three Gaussian pulses with 60 Hz bandwidth and separated by 20 ms each. The acquisition delay between the excitation and the signal acquisition was minimized to an echo time (TE) of 0.65 ms. A 4-kHz sampling rate FID was acquired with $T = 1024$ points followed by spoiler gradients for a TR of 355 ms. To avoid signal saturation considering the maximum T_1 value among metabolite to be 1400 ms [49], the excitation flip angle was set to 35 degrees. To avoid aliasing from signal outside the slab, two 30-mm-thick outer-volume saturation bands (OVS) were positioned right below and above the slab. The excited slab size was (A/P-R/L-H/F) 210 mm by 160 mm by 95 mm. The 3D encoding volume was set slightly larger to 210 mm by 160 mm by 105 mm again to prevent aliasing. An encoding matrix of $42 \times 32 \times 20$ resulted in a 131μl voxel volume (5 mm isotropic). A fast reference

water measurement was performed to determine the coil sensitivity profiles, with acquisition parameters identical to the main FID-MRSI sequence but without WET water suppression and with lower resolution $32 \times 24 \times 16$ (6.6 mm isotropic). The same encoding volume and slab were used but with 31-ms TR, 48 points in FID and a 5-degrees excitation flip angle. An anatomical 3D T_1-weighted MPRAGE sequence was also acquired during the session for navigation purpose and for anatomical segmentation of the volunteers' brain.

Sparse and random 3D phase-encoding MRSI raw data were acquired sparsely and randomly over the three-dimensional Fourier domain (k-space) to enable CS acceleration. The sequential phase encoding method of the FID-MRSI sequence allows for a straightforward implementation of the random k-space sampling. During sequence preparation, a 3D mask was computed containing only k-space coordinates to be acquired. Defining $q = \sqrt{(k_x/k_x^{max})^2 + (k_y/k_y^{max})^2 + (k_z/k_z^{max})^2}$, the random sampling of the 3D mask was constrained to a density distribution following q^{-1} but with a fully-sampled spheroid of radius $q \leq \frac{1}{5}$ (Fig. 1). During the sequence acquisition, following the preparation, FID MRSI data are acquired according to the 3D k-space mask.

B. MRSI data preprocessing and reconstruction model

Remaining water and lipid signal removal Residual water was removed using Hankel singular value decomposition (HSVD) method [50]. HSVD was applied separately to each coil element and time series in the acquired points of the k-space. The lipid suppression was performed in k-space on the signal from each coil element using a lipid subspace projection method [17] based on the metabolite-lipid spectral orthogonality hypothesis [15]. (The computation time of the residual water removal was below 60 min while the lipid suppression was computed within 2 min using Matlab R2018b (The MathWorks, Inc., Natick, Massachusetts, US) and 16 cores 3.00GHz Intel(R)Xeon(R)-E5 CPU). The methods are described in detail in previously published work [17].

CS-SENSE-LR reconstruction The CS approach requires reconstruction of the sparsely-sampled MRSI data with an appropriate model that maximizes data fidelity while constraining spatial sparsity in metabolite distributions [30, 31]. We employed here a

low-rank constrained model including total generalized variation (TGV) regularization [51]. We describe hereafter briefly the 3D extension of the CS-SENSE-LR reconstruction that was previously described in [17]. MRSI raw data measured by phased array coil element $c = 1, \ldots, N_c$ at time t and at k-space coordinate $\mathbf{k}$ can be expressed with the forward model

$$s_c(\mathbf{k}, t) = \int_{\Omega \subset \mathbb{R}^3} \mathrm{e}^{2\pi \mathrm{i} \mathbf{k} \cdot \mathbf{r}} C_c(\mathbf{r}) B(\mathbf{r}, t) \rho(\mathbf{r}, t) d\mathbf{r}, \tag{1}$$

with 3D spatial coordinates $\mathbf{r}$ integrated over Ω the spatial support of the measured object and $\rho(\mathbf{r}, t) \in \mathbb{C}$ the transverse magnetization. $C_c(\mathbf{r}) \in \mathbb{C}$ represent the coil sensitivity profiles and $B(\mathbf{r}, t) = \mathrm{e}^{2\pi \mathrm{i} t \gamma \Delta B_0(\mathbf{r})}$ the spatial frequency shift caused by $\gamma \Delta B_0(\mathbf{r})$, the magnetic field inhomogeneity map (in Hz). The goal of the reconstruction is to retrieve the original $\rho(\mathbf{r}, t)$ from the sparsely sampled signal $s_c(\mathbf{k}, t)$ knowing $C_c(\mathbf{r})$ and $\Delta B_0(\mathbf{r})$.

The low-rank assumption implies a decomposition of the transverse magnetization in K spatial and temporal components, $U_n(\mathbf{r})$, $V_n(t), n = 1, \ldots, K$:

$$\begin{aligned} \rho(\mathbf{r}, t) &= \sum_{n=1}^{K} U_n(\mathbf{r}) V_n(t) \\ &= \mathbf{U}(\mathbf{r}) \mathbf{V}(t), \end{aligned} \tag{2}$$

with the last line employing vectorial notation. Considering discrete spatial and temporal sampling points (N_t times points, N_k k-space acquisition points, N_x, N_y, N_z the reconstruction image size), $s_c(\mathbf{k}, t), \mathbf{U}(\mathbf{r})\mathbf{V}(t)$ become multi-dimensional arrays $\mathbf{s}, \mathbf{U}, \mathbf{V}$ with size respectively $(N_c \times N_k \times N_t)$, $(N_x \times N_y \times N_z \times K)$ and ($K \times N_t$). The forward model (1) reads then

$$\mathbf{s} = \mathcal{F}\mathcal{C}\mathcal{B}(\mathbf{UV}), \tag{3}$$

with the discrete Fourier transform operator $\mathcal{F}$ and $\mathcal{C}$ and $\mathcal{B}$ operators applying $C_c(\mathbf{r})$ and $B(\mathbf{r}, t)$ on discrete coordinates. After a first step consisting of remaining water removal and lipid signal suppression (described above) from $\mathbf{s}$, the discrete transverse magnetization $\rho = \mathbf{UV}$, is reconstructed $s_c(\mathbf{k}, t)$ with a 3D low-rank TGV model in [52]. The TGV minimization problem [51] enable determination of the spatial and temporal components

$$\arg\min_{\mathbf{UV}} \|\mathbf{s} - \mathcal{F}\mathcal{C}\mathcal{B}(\mathbf{UV})\|_2^2 + \lambda \textstyle\sum_{n=1}^{K} \mathrm{TGV}^2\{U_n\} \,. \tag{4}$$

The coil sensitivity profiles, $C_c(\mathbf{r})$ were determined from the fast reference water acquisition using ESPIRiT [53] and $\Delta B_0(\mathbf{r})$ was estimated using *multiple signal classification algorithm*

(MUSIC) [54] on the water signal from the same fast reference scan. By including coil sensitivity profiles and the TGV regularization that imposes sparsity in spatial first and second-order gradients, the CS-SENSE-LR reconstruction permits a faithful reconstruction of randomly sampled MRSI data [43, 55]. As a consequence of the sequence design, there is a delay between the excitation and the FID acquisition that causes a first order phase in the reconstructed spectra. To correct this effect, the first 2 missing points of the FID were estimated using a reverse autoregressive model [56] in each voxel of the reconstructed MRSI dataset $\rho = \mathbf{UV}$ individually.

LCModel Quantification In a last step, the reconstructed MRSI signal was fitted with LCModel [57, 59] to quantify metabolites voxel by voxel over the range of 1.0 to 4.2ppm. The LCModel basis was simulated using GAMMA package [58] and with parameters matching the acquisition sequence. The metabolites in the basis included: N-acetylaspartate, N-acetyl aspartylglutamate, creatine, phosphocreatine, glycerophosphocholine, phosphocholine, myo-inositol, scyllo-inositol, glutamate, glutamine, lactate, gamma-aminobutyric acid, glutathione, taurine, aspartate, alanine. LCModel results were expressed in institutional units that allow for comparison across metabolites and subjects (see LCModel documentation [59]).

Lipid suppression by orthogonality as performed in this study might distort the baseline at 2ppm below the NAA singlet peak. To optimize LCModel fitting in presence of this distortion a singlet broad and inverse peak was added to the basis. It was simulated at 2 ppm with 20 Hz width and a $e^{i\pi}$ phase (opposite to NAA singlet). LCModel quantification provides also estimates of spectrum SNR and a Cramer-Rao Lower bound (CRLB) for each metabolite. These are usually considered as spectral quality metrics, but for the present results reconstructed with the CS-SENSE-LR model prior to the LCModel fitting, these parameters might not assess data quality properly. Indeed, the accurate estimation of these parameters relies on the presence of measurement noise in the spectra. In the present work, the measurement noise is removed by using the denoising model. Therefore, CRLB values might be artificially low and SNR particularly high. Nevertheless, as they still reflect the fitting quality, they are provided in supplementary material. Instead, the average of the LCModel fit residuals is reported to describe spectral quality.

C. Experiments

CS acceleration demonstration To demonstrate the CS acceleration capability and to assess the metabolite maps reconstruction accuracy, a single MRSI acquisition without k-space undersampling was performed on a volunteer following the sequence details in II A with a full elliptical k-space encoding resulting in a 70 min acquisition. The raw data were first undersampled retrospectively to various extents to reproduce acceleration factors of $2, 3, 4, 5$ or 6 and following the same variable density undersampling than the actual accelerated acquisition (described in II A). After undersampling of the raw data, metabolite maps were reconstructed following all the steps from II B. The TGV regularization parameter λ in (4) was adjusted on the fully-sampled dataset (3×10^{-4}) and was kept the same for all acceleration factors. The reconstructed spectral quality was assessed at different accelerations and the fitting residuals of the LCModel were quantified as quality parameter. The resulting metabolite maps were compared qualitatively and quantitatively with a normalized root mean square error (RMSE) and structural similarity index (SSIM).

Healthy volunteers accelerated acquisition The FID-MRSI with accelerated acquisition was performed and reconstructed with the CS-SENSE-LR model on three volunteers to demonstrate reproducibility and robustness. Written informed consent was given by all the subjects before participation and the study protocol was approved by the institutional ethics committee. The FID-MRSI was acquired with an acceleration factor 3.5 (20 min, optimal factor determined by the CS acceleration demonstration) for all three volunteers and were reconstructed with the same regularization as retrospective acceleration case, i.e. $\lambda = 3 \times 10^{-4}$. The spectral quality was presented with selected reconstructed spectra from four locations: the cingulate grey matter (GM), the frontal white matter (WM), the caudate nucleus and the temporal GM with the corresponding LCModel fitting.

Brain-atlas regional analysis To illustrate the metabolite contrasts and their relation to the underlying anatomical structures, the 3D metabolite maps were co-registered to an anatomical brain atlas. For each participant, T_1-weighted anatomical scans were segmented into gray and white matter compartments by using the computational anatomy toolbox (CAT12; http://www.neuro.uni- jena.de/cat) as implemented in statistical parametric mapping (SPM12) software (https://www.fil.ion.ucl.ac.uk/spm/software/spm12/) run-

ning in Matlab R2018b (The MathWorks, Inc., Natick, Massachusetts, US). Native-space gray matter images were spatially normalized to the DARTEL template in MNI standard space created from 555 healthy control subjects from the IXI-database (http://www.brain-development.org). Masks for the cerebral lobes were generated using the Standard atlas [60] in WFU PickAtlas toolbox (https://www.nitrc.org/projects/wfu_pickatlas/) and spatially transformed in participants' native space by applying the inverse of the transformation matrix generated during the spatial normalization step. Subcortical gray matter structures were automatically segmented using Freesurfer version 6.0.0 [61]. The resulting anatomical atlases were first registered to the MRSI orientation (fig.5). The MRSI voxel size leads to partial voluming and a single MRSI voxel might contain contributions from several anatomical structure simultaneously. To cope with this partial volume effect and accurately estimate the concentration in each anatomical structure, a general linear model was employed for each metabolite [62]:

$$\mathbf{Y} = \sum_i \beta_i \mathbf{X_i} + \beta_0 + \epsilon \tag{5}$$

where $\mathbf{Y}$ is a vector made of the metabolite concentration in all voxels, $\mathbf{X_i}$ is a vector containing all partial-volume estimate (a value between 0 and 1) with i the index of the anatomical structures presented in fig.5, β_0 is the concentration intercept and ϵ represents normally distributed residual. Following the fit of the general linear model, the metabolite concentration in each anatomical structure corrected for the partial-volume is given by $\beta_i + \beta_0$. These values were computed for all three subjects and the mean ratios ($\frac{\text{tNAA}}{\text{tCre}}, \frac{\text{Cho}}{\text{tCre}}, \frac{\text{Ins}}{\text{tCre}}, \frac{\text{Glx}}{\text{tCre}}$) across subjects were compared with reported values [63–67]. A statistical analysis was performed across anatomical structures with the data of the three volunteers to highlight significant differences in metabolite concentration. An ANOVA was performed over the concentration results grouped by anatomical structure. Following this test, a multiple comparison was performed to investigate possible significant differences between individual structures.

III. RESULTS

The results of the in vivo MRSI data accelerated retrospectively to illustrate the CS performance are shown in fig.2 for the five major metabolites measured in 3T FID-MRSI: N-acetylaspartate + N-acetyl aspartylglutamate (tNAA), creatine + phosphocreatine (tCre), Choline moities metabolites (Cho) (choline, acetylcholine, phosphocholine and glycerophos-

phocholine), myo-inositol (Ins), glutamate + glutamine (Glx). The cortical layer is visible on tCr and Glx maps and the Cho distribution shows the highest signal intensity in frontal WM and the lowest values in occipital lobe. These spatial features remain clearly present while data are progressively randomly undersampled in the k-space from 50% to 17% (acceleration factor from 2 to 6). Although all datasets were reconstructed with the same regularization parameter value λ, metabolite images gradually loss fine detailed structures and show blurriness as the acceleration factor increases due to the lack of high k-space frequencies remaining sampled in the data. This is highlighted by the generally monotonic rise of RMSE and decrease of SSIM. This known effect of CS acceleration is further addressed in the Discussion. Thorough simulation of image reconstruction was performed to demonstrate this effect (results are presented in the supplementary material). It is demonstrated that a regularized model with optimal parameter minimizes the reconstruction error, whereas a strong acceleration of the data cannot be faithfully reconstructed without important loss of apparent resolution.

The RMSE and SSIM of each metabolite volume relative to the 'no acceleration' volume show monotonic behaviors close to a linear relation with the acceleration factor in agreement with previous publications [38, 55]. Among all metabolites Glx always shows the highest RMSE and lowest SSIM. This is probably due to the lower signal of glutamine and glutamate in comparison to other metabolite. tNAA also shows higher error and lower similarity in comparison to tCre or Cho. This is possibly relative to the lipid suppression that can affect baseline at 2 ppm and add variability in the tNAA quantification.

Spectra shown at two locations in the bottom of fig.2 exhibit no noticeable change with acceleration. Possible spectral distortion resulting of the acceleration would also reflect in an increase of fitting residuals. But the residuals root mean square (RMS) average over the brain remains practically constant.

The full tNAA, tCre, Cho, Ins and Glx maps resulting from the accelerated acquisition (i.e 3.5) are displayed for volunteer 1 in fig.3. The metabolite maps match the distribution features and have similar quality as for the retrospective acceleration by a factor 3 or 4 in fig.2. Volumes of Cho and Glx concentrations which display the sharpest contrasts, and four sample spectra are presented in fig.4 for each of the three volunteers. The concentrations variations observed in the metabolite maps translate into visual spectral variations. The frontal WM spectrum shows a clear higher Cho peak with respect to other three lo-

cations and Cingulate GM and Temporal GM spectra present markedly higher Glx signal than Frontal WM and Caudate. These visual landmarks are noticeable for all three volunteers. The metabolite concentration ratio maps of the same measurements are shown in supplementary Fig.S9. In addition, CRLB and SNR maps of these results are presented in supplementary Fig.S10 but should be interpreted with caution. Indeed, their accuracy might be affected by the reconstruction process as described in the Methods. To validate the quantification in institutional units with respect to the water reference signal, MRSI data were measured, reconstructed and quantified on a homogeneous metabolite solution phantom (MRS Braino phantom, GE Medical Systems, Milwaukee, WI, USA). The resulting metabolite map (supplementary Fig.S16) exhibit homogeneity over the whole phantom.

The spectra shown in fig.4 and fig.2 exhibit high SNR thanks to the low-rank constraint and a narrow linewidth due to the small voxel size in addition to the B_0 fieldmap correction included in the CS-SENSE-LR model. Mean whole-brain SNR estimated by LCModel was 14.2, 12.7 and 12.6 for volunteers 1 to 3. The mean spectral full width at half maximum was 5.67 Hz, 5.46 Hz and 5.19 Hz for the same subjects. The baseline distortion due to the lipid suppression by orthogonality is visible as a pit at 2 ppm forming a 'W' shape with the NAA peak. Nevertheless, the distortion is well fitted by the inverse broad peak added to the basis and the resulting baseline is smooth. This point is further addressed in the Discussion.

The anatomical segmentation of 3D metabolite maps for volunteer 1 is illustrated in fig.5. Concentrations of each anatomical region computed from eq.(5) are reported in fig.6 and illustrate the consistency of the anatomical contrasts: for all volunteers, the distribution of metabolite concentrations follow similar patterns. For tNAA, cortical concentrations tend to be lower in temporal lobes while subcortical concentrations are relatively high in the thalamus. Similarly, tCre concentrations are lower in temporal lobes than in other cortical regions. There is also a systematic difference in tCre between GM and WM. For Cho, plots show a lower concentration in GM than in WM as well as a high concentration in brain stem, hippocampus and amygdala. In contrast to Cho, Glx exhibits a consistent and markedly higher concentration in GM than in WM. Distribution of Ins concentrations follow similar GM-WM contrast to tCre. Concentrations in the cerebellum are marked by high concentration of tCre, Glx and Ins. The ratios of metabolite concentrations in each anatomical region, averaged across subjects are presented in fig.7. Values from left and right hemisphere were combined to facilitate comparison with results from the literature [63–67].

Globally, results of tNAA/tCre, Cho/tCre and Glx/tCre match the previously reported ratio values with differences that are in the range of what has been previously published, despite tNAA/tCre, Cho/tCre values are in the highest reported values and Glx/tCre in the lowest. The GM-WM contrast that is reported in the literature for all metabolite ratios, is also observed in the present study. Ins/tCre values are systematically larger than the literature results although the GM-WM contrast here is comparable. Results of the statistical analyses of differences across brain regions are presented in supplementary Fig.S15. The ANOVA analysis exhibited a significant difference across regions in all the metabolites (p-value given in the title of each figure). The results of the multiple comparison testing are presented as matrices for each metabolite. Significant differences (corrected $p < 0.05$) are consistent with the qualitative results described above. Cerebellum concentration is significantly higher than numerous other structures for tCre, Cho and Glx. The cortical GM regions are significantly different from WM and deep GM structures regarding Glx and tCre. Ins and tNAA show fewer significant differences between deep GM structures or between deep GM structures and lobe values.

IV. DISCUSSION

There is a strong need for the whole-brain mapping of the metabolite distributions in fine details and within an acceptable time frame to allow its inclusion in scanning protocols running on regular 3T MR systems. For the first time, the unique combination of FID-MRSI with CS-SENSE-LR made the reconstruction of high-contrast possible and high-resolution 3D metabolite volumes following an acquisition limited to 20 min on a clinical 3T MRI.

The whole-brain approach coupled with the high-resolution (i.e. 5 mm isotropic) of the reconstructed volumes allowed a quantitative analysis of the brain metabolites in all brain regions. Results from the 3 volunteers showed the same patterns of contrast between cerebral lobes, subcortical structures and GM/WM segments for each metabolite, suggesting a good consistency of the measures.

The performance of the CS-SENSE-LR model in reconstructing undersampled dataset as depicted in fig.2 is demonstrated by the retrospective acceleration (or k-space undersampling) of a fully sampled 3D FID-MRSI. The random k-space spheroid sampling following a radius^{-1} distribution rule only affects the resulting spatial metabolite distributions without

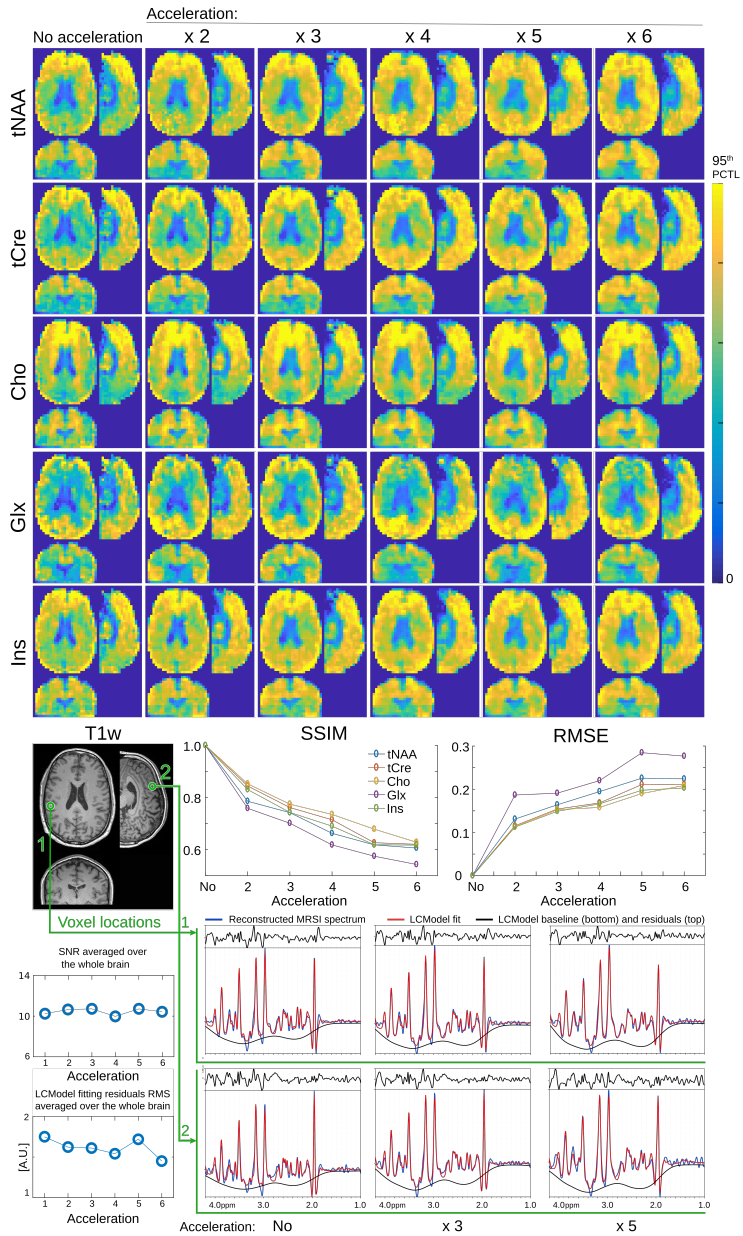

FIG. 2. Top, 3D FID-MRSI reconstructed metabolite volumes with retrospective acceleration. The fully sampled acquisition (No acceleration) was acquired in 70 min and acceleration factors correspond to k-space undersampling and reducing acquisition time accordingly (e.g. x3: 24 min, x6: 12 min). The color map was scaled individually for each metabolite range from 0 to the 95th percentile. Bottom, the normalized root mean squar error (RMSE) and structural similarity index (SSIM) computed for each metabolite map at all acceleration factors relative to the unaccelerated result. Bottom, sample spectra from 2 distinct locations are displayed and exhibit very little variation with the acceleration (no, 3, 5). The LCModel fit are shown with the fitting residuals. The root mean square (RMS) of the residuals averaged over the whole brain remains constant with the acceleration (bottom plot).

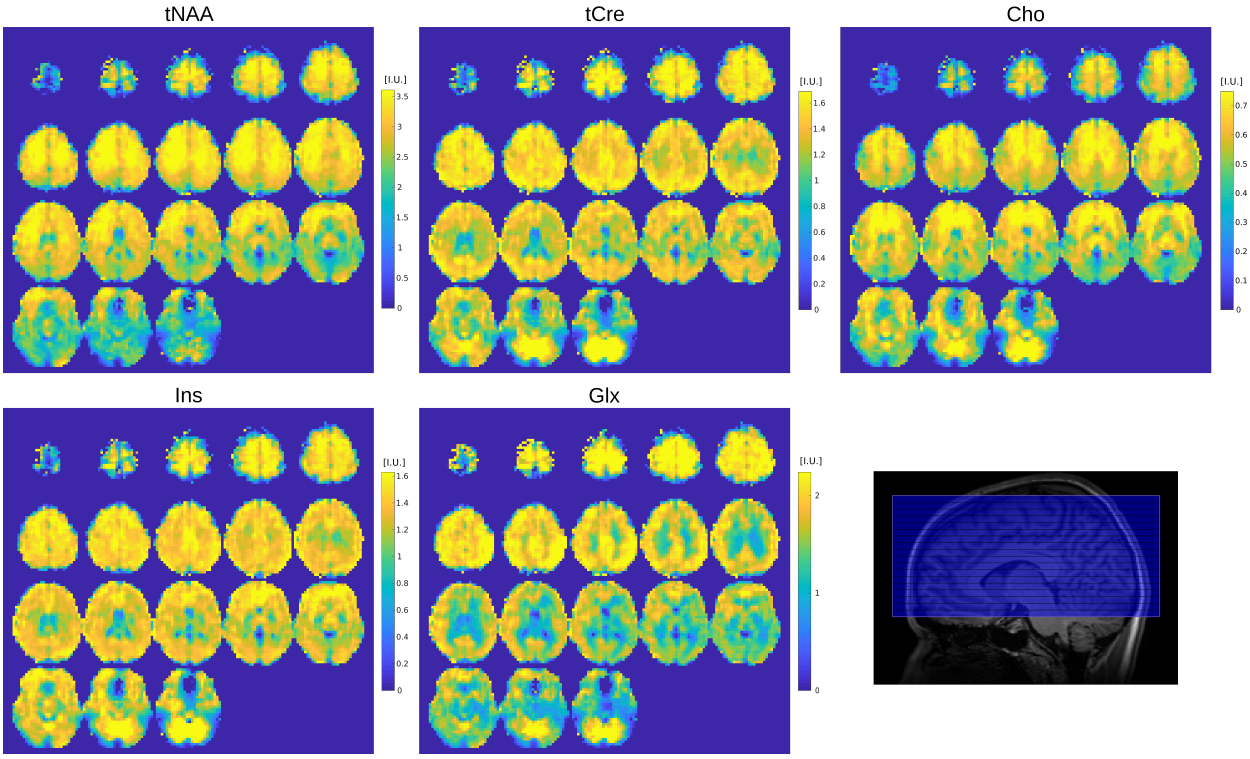

FIG. 3. CS-SENSE-LR 3D FID-MRSI measured on a healthy volunteer (volunteer 1) with 5 mm isotropic resolution in 20 min with acceleration factor 3.5, resulted in tNAA, tCre, Cho, Ins and Glx maps. Color scale for each map is given in institutional units. Sagittal T_1-weighted image (bottom right) show the location of the excitation slab (blue overlay).

downgrading the spectral quality. Indeed, the variable density undersampling scheme mostly removes acquisition points at the periphery of the k-space while preserving the center that contains the majority of the signal. As a consequence, spectral SNR is practically preserved by acceleration scheme. This reconstruction property was highlighted by the qualitative and quantitative analysis of spectra after the retrospective acceleration in fig.2 and was also reported in a previous publication [38]. When acceleration factor is increased, fine-scale details are gradually disappearing. As stated before, this artifact is caused by the undersampling of the high k-space frequencies [43, 44]. The same effect could be reproduced with simulation data on two reference images, supplied as supplementary material (fig.S3, S4, S7 and S8). For high acceleration factors images show erosion of small structures even when the regularization parameter value is optimal. This non-uniform effect might differ for some fine-scale features or large image elements [44]. As illustrated by the increase of RSME and decrease of SSIM, this effect on the metabolite maps is already present at small accelera-

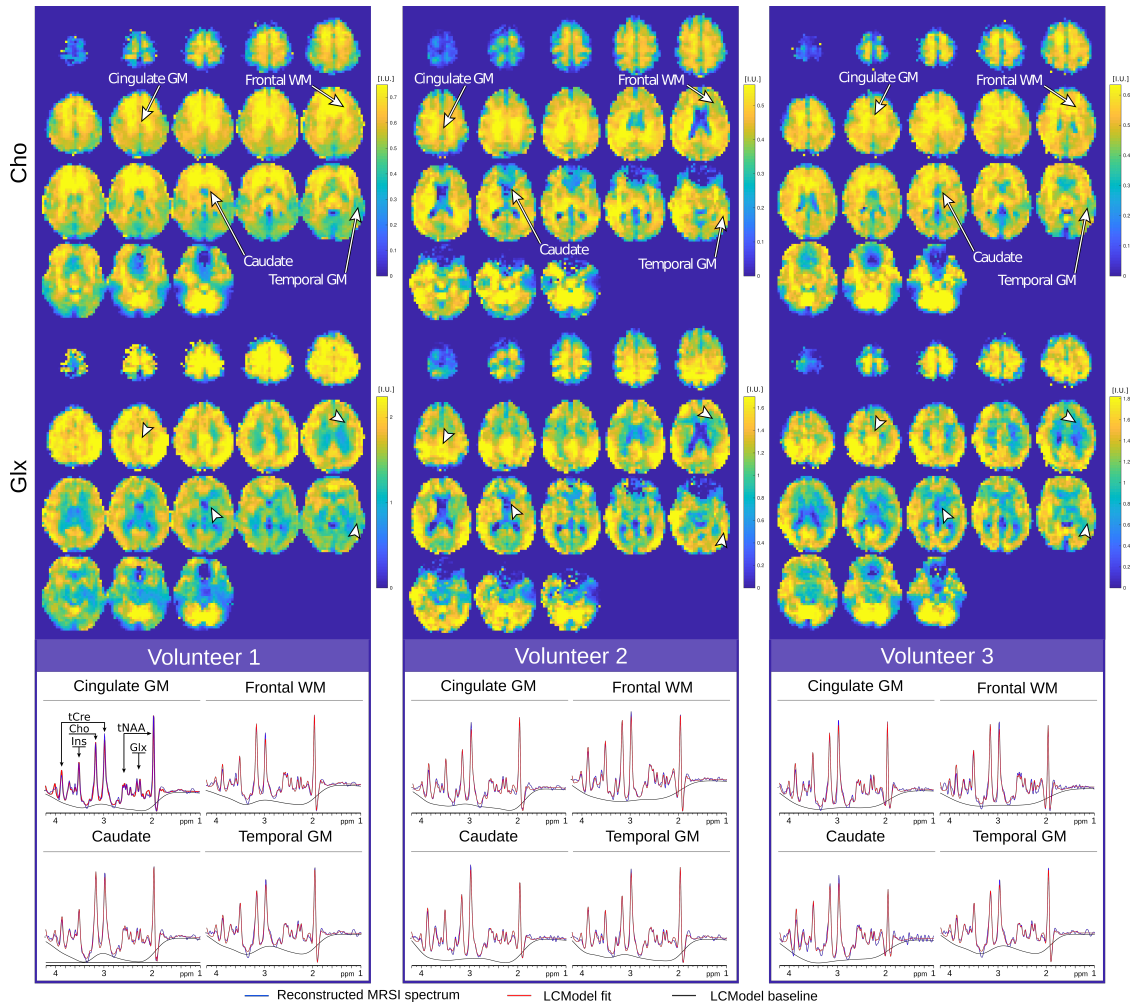

FIG. 4. Comparison of high-contrast Cho and Glx 3D maps measured with CS-SENSE-LR FID-MRSI on three healthy volunteers (volunteer 1,2 and 3) with 5 mm isotropic resolution in 20 min (acceleration factor 3.5). Color scale is given in institutional units for the respective metabolite concentration. Samples spectra originating from four distinct locations are shown for each volunteer. Cho and Glx signal amplitude in the spectra match the metabolite distribution observable on the maps. Metabolite ratio maps of the same volunteers and the corresponding Cramer-Rao lower bound (CRLB) and SNR maps estimated by LCModel are shown in supplementary Fig.S10.

tion factor and becomes increasingly visible. The aim of the retrospective analysis shown in fig.2 is to find the right balance between an acceptable loss in metabolite map quality and a substantial gain in acquisition time. Based on the present results, an acceleration factor of 3.5 was found to be optimal. Higher acceleration factor is accompanied by a loss of apparent resolution and illustrates that the method allow only low to moderate acceleration

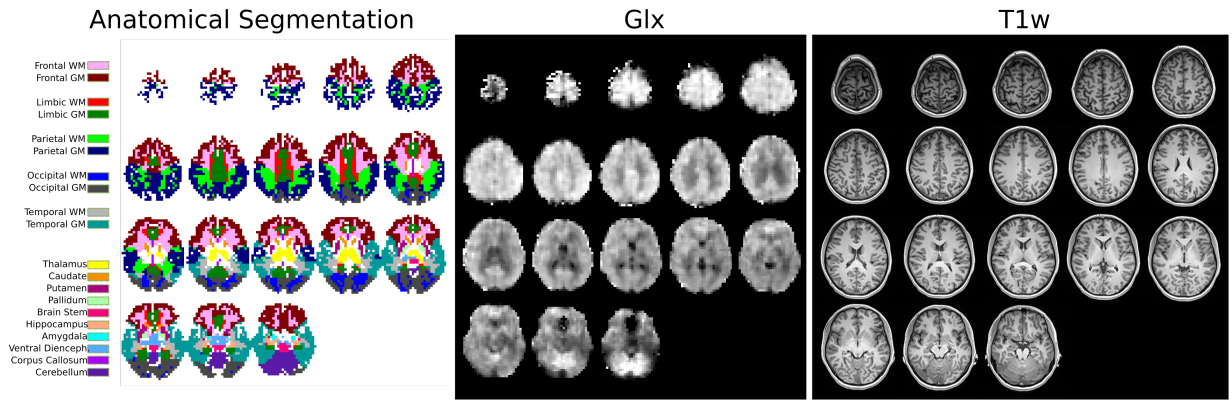

FIG. 5. Left, the anatomical atlas registered to volunteer 1 is shown with voxel labeling corresponding to the dominant partial-volume. Center, Glx concentration 3D map is shown for qualitative comparison in a grey scale and, right, the MPRAGE T_1-weighted images used to segment the volunteer anatomic parts.

in comparison to other acceleration methods [13, 14, 24].

The TGV regularization parameter used in the reconstruction was adjusted to $\lambda = 3 \times 10^{-4}$ by gradually increasing the regularization until disappearance of noise-like artifact in the metabolite maps [51]. An L-curve was computed for one of the volunteer dataset (supplementary Fig.S14) and $\lambda = 3 \times 10^{-4}$ matches the point of maximum curvature that is also considered as the optimal regularization parameter value [68]. The optimal value found was slightly lower than the previously found value in the 2D case ($\lambda = 10^{-3}$ in [17]). However, this same value was observed to be optimal for all 4 volunteer datasets. Therefore, the regularization parameter seems to depend mainly on the MRSI protocol and might require some minor adjustment when the slab thickness, the resolution, the flip-angle or other acquisition parameters are modified. The number of components in the model (K in (2)) was chosen empirically as follows. The initial estimation of the components were computed with SVD performed on the adjoint solution of the MRSI data. These initial components were then visualized and K was chosen such that all U_n, V_n for $n > K$ contain mainly noise. This upper limit was found to be consistently ≈ 35 for all subjects and was safely set to 40. For $K < 20$, key metabolite features tend to disappear and there was no noticeable difference in the resulting metabolite maps with K chosen between 40 and 20. Therefore, choosing $K = 40$ was considered safe. The MRSI reconstruction including all pipeline steps takes approximately 12 hours to complete using Matlab R2018b (The

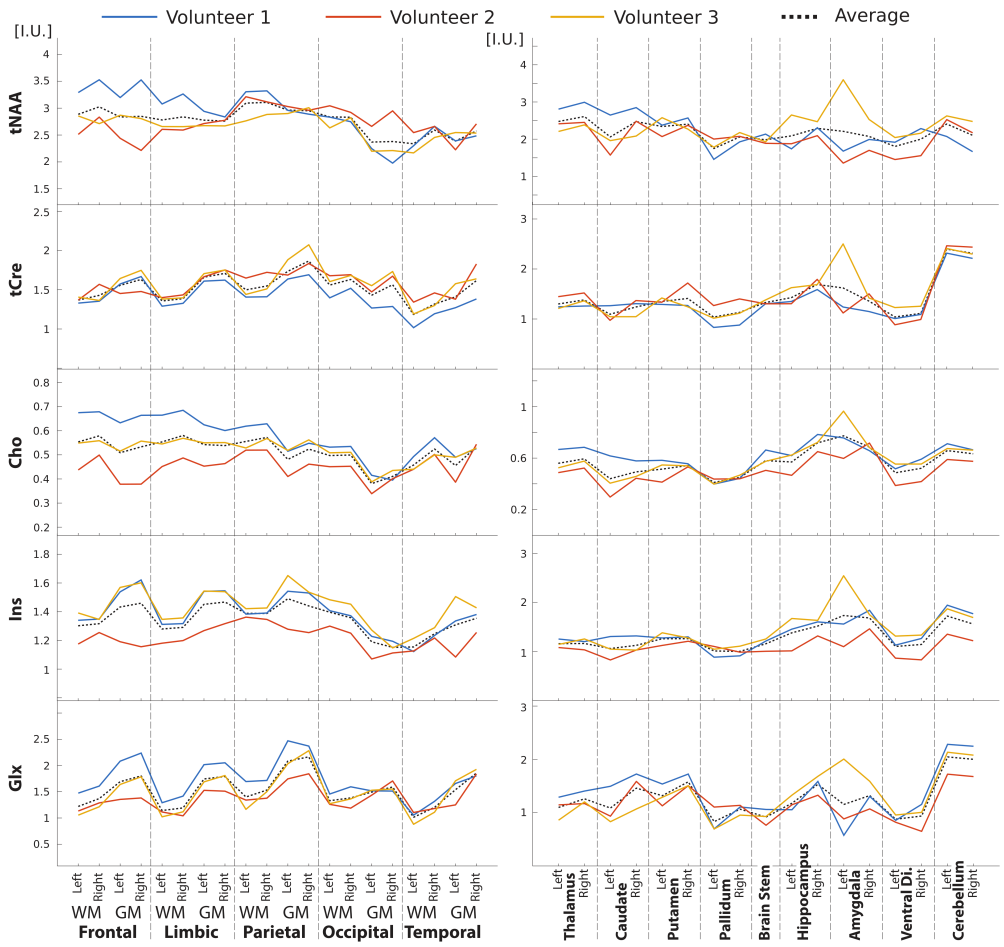

FIG. 6. Atlas metabolite content across three healthy volunteers based on anatomical segmentation (fig.5). Lines correspond to the metabolite concentration estimated using eq.(5) for all anatomical area for each of the three volunteers. The dashed line represents the mean values across the three volunteers. Metabolite levels are expressed in institutional units. Left plots represent relative concentrations in WM or GM in each cerebral lobe while right plots show relative concentrations in the deep GM.

MathWorks, Inc., Natick, Massachusetts, US) and 16 cores 3.00GHz Intel(R)Xeon(R)-E5 CPU.

The acceleration factor 3.5 of our protocol provides a drastically shorter acquisition (20 min) in comparison to the fully sampled protocol (70 min). However, the MRSI acquisition, even accelerated, remains markedly long and is therefore susceptible to subject motion. While no motion correction or compensation were used in this study, the implementation of an interleaved imaging-based volumetric navigators could be expected to further

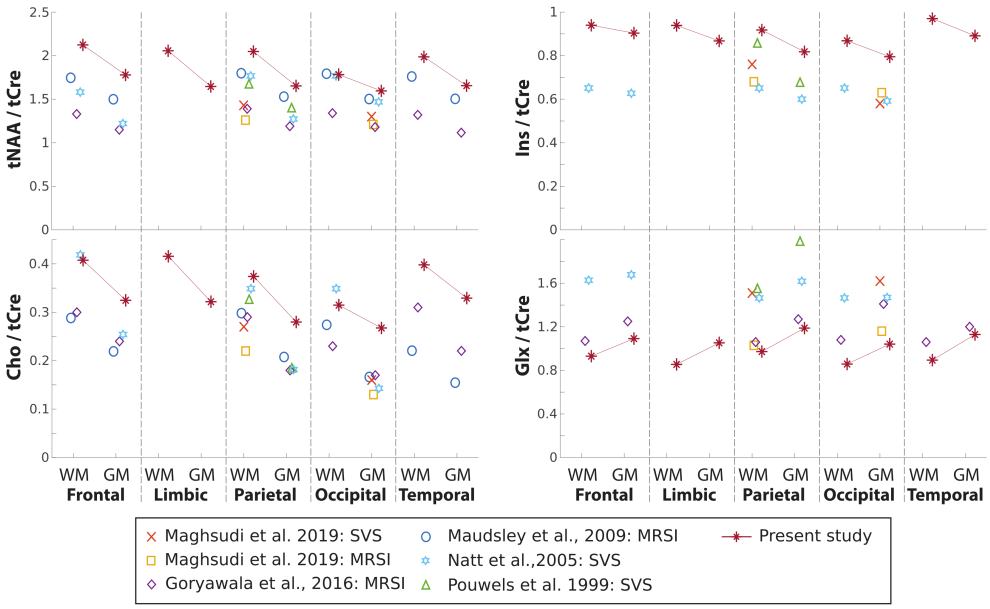

FIG. 7. Comparison of the atlas metabolite-ratio content to previously published results. Line-connected points correspond to the metabolite average ratio from volunteers 1 to 3 (individual data presented in fig.6). The legend indicates the corresponding study and the type of acquisition: whole-brain MRSI or sing voxel spectroscopy (SVS)

improve the measurement accuracy and prevent possible motion artefact as shown in [40].

Although the lipid suppression by orthogonality performed as pre-processing efficiently removes any lipid signal from the brain spectra, it creates a specific distortion of the baseline at 2 ppm particularly visible in the spectra of fig.2 and less marked in fig.4. The distortion may strongly affect LCModel fitting performance that compensate the pit by an unrealistic 1st order phase correction impacting the quantification stability. We partially solved the issue by introducing a broad inverse peak in the LCModel basis that allows the distortion pit to be fitted as a negative peak while preserving the spectral phase and baseline estimation. While not being the scope of this article, this coping technique might alter the quantification of NAA and NAAG and further investigations are necessary to ascertain the fitting of these metabolites. The low-rank reconstruction model guides the reconstruction towards a solution containing the dominant components in the signal. Therefore, the lipid signal suppression must be performed before the reconstruction. Otherwise, most of the model components would contain lipid signal that overcomes the metabolite signal by several order of magnitude, leading to inacurate metabolite mapping reconstruction. Furthermore,

in order to prevent this baseline distortion, the lipid suppression by orthogonality could be replaced by other sequence-based lipid removal methods such as saturation radio-frequency pulses [42] or pulsed magnetic field gradients [69] that may better preserve the metabolite signal around 2 ppm. The CS-SENSE-LR acquisition and reconstruction pipeline could be directly applied to these techniques. An additional limitation of the lipid suppression by orthogonality performed during pre-processing is the removal of the macromolecule (MM) signal. In contrast to the metabolite signal, the MM signal does not appear to be spectrally orthogonal to skull lipid signal contrarily to the metabolite signal. The MM signal is identified as lipid and is removed during the lipid suppression step. Measurement of MM with the presented technique would require the replacement of the lipid suppression by orthogonality with a sequence based lipid suppression method [42, 69]. The use of the FID-MRSI sequence enables the acquisition of MRSI data with an ultra-short TE. This could be advantageous because a TE $<$ 1ms prevents essentially any T_2 relaxation weighting in the measured data. In contrast, the short TR employed with FID-MRSI in the present study may result in T_1-weighting of the metabolite signal. Indeed the steady-state magnetization of each metabolite consecutive to the reduced TR depends on the respective metabolite T_1 value. Following previously published results [70, 71], brain metabolite T_1 values are expected to range from 1000 to 1400 ms, and the steady-state magnetization may therefore vary by $\pm 7\%$ (see supplementary Fig.S18). Nevertheless, this possible T_1-weighting represents a signal variation smaller than the contrast observed in the metabolite maps (see e.g. fig.6). The sample spectra in fig.2 and fig.4 show a particular high Ins peak at 3.9 ppm. Compared to other MRS sequences, ultra-short TE FID-MRSI sequence maximizes the signal of Ins with respect to other metabolites. The Ins signal is the result of overlapping multiplets evolving with strong proton J-coupling. With long TE, the J-coupling results in modulation and dephasing of each multiplet peak, leading to a lower apparent Ins signal at 3.9 ppm. On the contrary, with TE $<$ 1ms in the present study, there is practically no modulation time between the excitation and the acquisition, and the Ins signal is maximum. A simulation illustrating this effect is shown in supplementary Fig.S19.

The 3D metabolite distributions observed over the whole brain in fig.2, 3 and 4 contained features and contrast described in III that are in agreement with previous publications. Thus, the distribution of tNAA, tCr, Cho exhibit similar pattern to the published data in [65, 72] and Glx in [10, 40, 66]. Ratio results in the present study are comparable with

those reported in the literature. In particular, the GM-WM contrast previously observed across healthy brains in most metabolites is reproduced by the present study. Differences are observed in the Ins/tCre values that are systematically higher in our results. Also Glx/tCre seems systematically low, although considering the variability across previously reported results, it remains in good agreement and particularly with the data from Goryawala *et al.* [66]. These discrepancies could be caused by the difference in acquisition sequence. All previously reported results were acquired with a spin echo sequence and with a significantly longer TE (>20 ms). As described above, the difference in TE might greatly influence the quantification of some J-coupled metabolites. To date, there is no other FID-MRSI results reported on atlas for comparison. The magnitude and the consistency of these contrasts are emphasized by the statistical analysis of the data across the three subjects. Numerous significant differences were found between regions exhibiting high contrast in the metabolite maps (see supplementary Fig.S15). Cerebellum was only partially covered by the VOI but the results of the anatomical analysis are in agreement with previously reported data that showed a high levels of tCre, Glx and Ins in this structure of the hindbrain [63, 64]. With the presented acquisition over the whole-brain, an extension of the VOI to cover the entire cerebellum would cause a degradation of the data quality because of shimming performance limitations. Nevertheless, recent work showed the feasibility of acquiring MRSI over the whole cerebellum [73]. Our results remain senstitive to B_0-field inhomogeneity that results in local linewidth increase. This effect is visible in the lower sections of the metabolite maps, B_0 fieldmaps and linewidth maps (fig.4, supplementary Fig.S12, supplementary Fig.S11). A cautious assessment of the LCModel spectral fit would notice the presence some visible residuals around 3.1 and 3.3 ppm in the fit of the displayed spectra in fig.2 and 4. These residuals might be caused by a discrepancy in the peak shape between the reconstructed MRSI datasets and the reference LCModel basis set. A possible cause of this difference might be the 1st order spectral phase correction by estimation of the first FID missing point as described in the methods. Considering the aforementioned issues, the spectral quality is particularly good thanks to the CS-SENSE-LR constrained reconstruction, with a mean linewidth below 6 Hz for all three volunteers and a LCModel-estimated SNR above 12 for all of them. These encouraging results spark interest for applications of the CS-SENSE-LR reconstruction to other low-SNR MRSI acquisition strategies such as MEGA spectral-editing technique [74] or fast spatial-spectral encoding [14].

The consistency of the segmentation results across subject in fig.6 illustrates qualitatively the sensitivity of the technique but an actual reproducibility study would be useful to assess the measurement variability and disentangle intersubject physiological difference from inter scan methodological variability.Based on our presented results, an application to SSE with undersampled trajectory should be considered and would yield even shorter acquisition time for equivalent or higher resolution. The acquisition-reconstruction method proposed in this study compares to other published work on full brain MRSI at 3T [24, 39, 40, 75]. The strategy presented here relies on a full Cartesian encoding of the Fourier domain whereas other approaches include SSE encoding. Compared to SSE which allows one spatial dimension to be encoded during FID readout in combination with a 2D phase encoding, a disadvantage of the fully Cartesian encoding may be the longer acquisition time required by the 3D phase encoding. With SSE technique, one dimension is encoded during readout and combined with a 2D phase encoding. Our results on the CS acceleration capability gives us an acceleration factor upper limit of 4. Given the constraint to measure the 3D Cartesian MRSI in reasonable acquisition time (20 min), the method would be generally limited to a resolution of 5-mm isotropic voxel whereas previous work employing SSE already exceeded this resolution at 3T [24, 40]. Nevertheless, one advantage of the fully Cartesian approach is the simple implementation of the encoding and its low requirement on gradient system performance which might minimize encoding inaccuracy. The CS-SENSE-LR model used for the undersampled MRSI reconstruction might represent a limitation in the application of the method as it requires a dozen of hours for the full processing. However, hardware improvement, software optimization, parallelization and algorithm development could reduce dramatically the processing time.

To conclude, a novel acquisition-reconstruction scheme, combining FID-MRSI with CS-SENSE-LR, makes 3D spectroscopic imaging of the whole human brain in high-resolution on a 3T system possible. The reconstructed metabolite volumes showed high anatomical contrast and high levels of features in 5 mm isotropic resolution. The resulting spectral quality demonstrated the efficiency of the model reconstruction for SNR enhancement and B_0 field map correction. Acceleration by random k-space undersampling allowed a dramatic reduction of the acquisition time from 70 to 20 min which makes its implementation in clinical or research protocols feasible. As proof of concept, metabolite volumes from three volunteers were segmented into anatomical lobes and substructures. The resulting contrast

observed quantitatively is the counterpart of the metabolite features visible on 3D metabolite maps and are consistent through all three volunteers.

V. ACKNOWLEDGMENTS

PK is supported by a fellowship from the Adrian and Simone Frutiger Foundation.

---

[1] Duyn J H, Gillen J, Sobering G, Zijl P C, Moonen C T. Multisection proton MR spectroscopic imaging of the brain. *Radiology.* 1993;188:277–82.

[2] Tedeschi Gioacchino, Bertolino A., Righini A., et al. Brain regional distribution pattern of metabolite signal intensities in young adults by proton magnetic resonance spectroscopic imaging *Neurology.* 1995;45:1384–1391.

[3] Posse S, DeCarli C, Le Bihan D. Three-dimensional echo-planar MR spectroscopic imaging at short echo times in the human brain. *Radiology.* 1994;192:733–738.

[4] Adalsteinsson Elfar, Irarrazabal Pablo, Topp Simon, Meyer Craig, Macovski Albert, Spielman Daniel M.. Volumetric spectroscopic imaging with spiral-basedk-space trajectories *Magnetic Resonance in Medicine.* 1998;39:889–898.

[5] Ebel Andreas, Maudsley Andrew A.. Improved spectral quality for 3D MR spectroscopic imaging using a high spatial resolution acquisition strategy *Magnetic Resonance Imaging.* 2003;21:113–120.

[6] Mansfield P.. Spatial mapping of the chemical shift in NMR *Magnetic Resonance in Medicine.* 1984;1:370–386.

[7] Ebel Andreas, Schuff Norbert. Accelerated 3D echo-planar spectroscopic imaging at 4 Tesla using modified blipped phase-encoding *Magnetic Resonance in Medicine.* 2007;58:1061–1066.

[8] Otazo Ricardo, Tsai Shang-Yueh, Lin Fa-Hsuan, Posse Stefan. Accelerated short-TE 3D proton echo-planar spectroscopic imaging using 2D-SENSE with a 32-channel array coil *Magnetic Resonance in Medicine.* 2007;58:1107–1116.

[9] Zhu Xiaoping, Ebel Andreas, Ji Jim X., Schuff Norbert. Spectral phase-corrected GRAPPA reconstruction of three-dimensional echo-planar spectroscopic imaging (3D-EPSI) *Magnetic Resonance in Medicine.* 2007;57:815–820.

[10] Moser Philipp, Bogner Wolfgang, Hingerl Lukas, et al. Non-Cartesian GRAPPA and coil combination using interleaved calibration data – application to concentric-ring MRSI of the human brain at 7T *Magnetic Resonance in Medicine.* 2019;82:1587–1603.

[11] Lam Fan, Ma Chao, Clifford Bryan, Johnson Curtis L, Liang Zhi-Pei. High-resolution 1H-MRSI of the brain using SPICE: Data acquisition and image reconstruction *Magnetic Resonance in Medicine.* 2016;76:1059–1070.

[12] Barker Peter B., Lin Doris D.M.. In vivo proton MR spectroscopy of the human brain *Progress in Nuclear Magnetic Resonance Spectroscopy.* 2006;49:99–128.

[13] Vidya Shankar Rohini, Chang John C., Hu Houchun H., Kodibagkar Vikram D.. Fast data acquisition techniques in magnetic resonance spectroscopic imaging *NMR in Biomedicine.* 2019;32:e4046.

[14] Bogner Wolfgang, Otazo Ricardo, Henning Anke. Accelerated MR spectroscopic imaging—a review of current and emerging techniques *NMR in Biomedicine.* 2020.

[15] Bilgic Berkin, Gagoski Borjan, Kok Trina, Adalsteinsson Elfar. Lipid suppression in CSI with spatial priors and highly undersampled peripheral k-space *Magnetic Resonance in Medicine.* 2013;69:1501-11.

[16] Ma Chao, Lam Fan, Johnson Curtis L., Liang Zhi Pei. Removal of nuisance signals from limited and sparse1H MRSI data using a union-of-subspaces model *Magnetic Resonance in Medicine.* 2016.

[17] Klauser Antoine, Courvoisier Sebastien, Kasten Jeffrey, et al. Fast high-resolution brain metabolite mapping on a clinical 3T MRI by accelerated 1H-FID-MRSI and low-rank constrained reconstruction *Magnetic Resonance in Medicine.* 2019;81:2841–2857.

[18] Tsai Shang Yueh, Lin Yi Ru, Lin Hsin Yu, Lin Fa Hsuan. Reduction of lipid contamination in MR spectroscopy imaging using signal space projection *Magnetic Resonance in Medicine.* 2019.

[19] Eslami Ramin, Jacob Mathews. Robust reconstruction of MRSI data using a sparse spectral model and high resolution MRI priors *IEEE Transactions on Medical Imaging.* 2010;29:1297–1309.

[20] Nguyen Hien M, Peng Xi, Do Minh N, Liang Zhi-Pei. Denoising MR spectroscopic imaging data with low-rank approximations *IEEE Trans Biomed Eng.* 2013;60:78–89.

[21] Otazo Ricardo, Lin Fa-Hsuan, Wiggins Graham, Jordan Ramiro, Sodickson Daniel, Posse Stefan. Superresolution parallel magnetic resonance imaging: application to functional and spectroscopic imaging *Neuroimage.* 2009;47:220–230.

[22] Kasten Jeffrey, Klauser Antoine, Lazeyras François, Van De Ville Dimitri. Magnetic resonance spectroscopic imaging at superresolution: Overview and perspectives *J Magn Reson.* 2016;263:193–208.

[23] Lam Fan, Ma Chao, Clifford Bryan, Johnson Curtis L, Liang Zhi-Pei. High-resolution (1) H-MRSI of the brain using SPICE: Data acquisition and image reconstruction *Magn Reson Med.* 2015.

[24] Lam Fan, Li Yudu, Guo Rong, Clifford Bryan, Liang Zhi Pei. Ultrafast magnetic resonance spectroscopic imaging using SPICE with learned subspaces *Magnetic Resonance in Medicine.* 2020;83:377–390.

[25] Maudsley A. A., Hilal S. K., Perman W. H., Simon H. E.. Spatially resolved high resolution spectroscopy by "four-dimensional" NMR *Journal of Magnetic Resonance (1969).* 1983;51:147–152.

[26] Pohmann R., Kienlin M., Haase A.. Theoretical Evaluation and Comparison of Fast Chemical Shift Imaging Methods *Journal of Magnetic Resonance.* 1997;129:145–160.

[27] Henning Anke, Fuchs Alexander, Murdoch James B, Boesiger Peter. Slice-selective FID acquisition, localized by outer volume suppression (FIDLOVS) for (1)H-MRSI of the human brain at 7 T with minimal signal loss *NMR Biomed.* 2009;22:683–696.

[28] Bogner W., Gruber S., Trattnig S., Chmelík M.. High-resolution mapping of human brain metabolites by free induction decay 1H MRSI at 7 T *NMR in Biomedicine.* 2012;25:873–882.

[29] Sabati Mohammad, Zhan Jiping, Govind Varan, Arheart Kristopher L., Maudsley Andrew A.. Impact of reduced k-space acquisition on pathologic detectability for volumetric MR spectroscopic imaging *Journal of Magnetic Resonance Imaging.* 2014;39:224–234.

[30] Donoho D.L.. Compressed sensing *IEEE Transactions on Information Theory.* 2006;52:1289–1306.

[31] Michael Lustig, David Donoho, M. Pauly John. Sparse MRI: The application of compressed sensing for rapid MR imaging *Magnetic Resonance in Medicine.* 2007;58:1182-1195.

[32] Hu Simon, Lustig Michael, Balakrishnan Asha, et al. 3D compressed sensing for highly accelerated hyperpolarized 13 C MRSI with in vivo applications to transgenic mouse models of

cancer *Magnetic Resonance in Medicine.* 2010;63:312–321.

[33] Hu Simon, Lustig Michael, Chen Albert P, et al. Compressed sensing for resolution enhancement of hyperpolarized 13C flyback 3D-MRSI *J Magn Reson.* 2008;192:258–264.

[34] Geraghty Benjamin J, Lau Justin Y C, Chen Albert P, Cunningham Charles H. Accelerated 3D echo-planar imaging with compressed sensing for time-resolved hyperpolarized (13) C studies *Magn Reson Med.* 2016.

[35] Geethanath Sairam, Baek Hyeon-Man, Ganji Sandeep K., et al. Compressive Sensing Could Accelerate 1 H MR Metabolic Imaging in the Clinic *Radiology.* 2012;262:985–994.

[36] Chatnuntawech Itthi, Gagoski Borjan, Bilgic Berkin, Cauley Stephen F., Setsompop Kawin, Adalsteinsson Elfar. Accelerated 1 H MRSI using randomly undersampled spiral-based k-space trajectories *Magnetic Resonance in Medicine.* 2015;74:13–24.

[37] Wilson Neil E., Iqbal Zohaib, Burns Brian L., Keller Margaret, Thomas M. Albert. Accelerated five-dimensional echo planar J-resolved spectroscopic imaging: Implementation and pilot validation in human brain *Magnetic Resonance in Medicine.* 2016;75:42–51.

[38] Nassirpour Sahar, Chang Paul, Avdievitch Nikolai, Henning Anke. Compressed sensing for high-resolution nonlipid suppressed 1H FID MRSI of the human brain at 9.4T *Magnetic Resonance in Medicine.* 2018.

[39] Lecocq Angèle, Le Fur Yann, Maudsley Andrew A., et al. Whole-brain quantitative mapping of metabolites using short echo three-dimensional proton MRSI *Journal of Magnetic Resonance Imaging.* 2015;42:280–289.

[40] Moser Philipp, Eckstein Korbinian, Hingerl Lukas, et al. Intra-session and inter-subject variability of 3D-FID-MRSI using single-echo volumetric EPI navigators at 3T *Magnetic Resonance in Medicine.* 2019:mrm.28076.

[41] Schirda Claudiu V., Zhao Tiejun, Yushmanov Victor E., et al. Fast 3D rosette spectroscopic imaging of neocortical abnormalities at 3 T: Assessment of spectral quality *Magnetic Resonance in Medicine.* 2018;79:2470–2480.

[42] Esmaeili Morteza, Bathen Tone F., Rosen Bruce R., Andronesi Ovidiu C.. Three-dimensional MR spectroscopic imaging using adiabatic spin echo and hypergeometric dual-band suppression for metabolic mapping over the entire brain *Magnetic Resonance in Medicine.* 2017;77:490–497.

[43] Liang Dong, Liu Bo, Wang Jiunjie, Ying Leslie. Accelerating SENSE using compressed sensing. *Magnetic resonance in medicine.* 2009;62:1574–84.

[44] Sharma Samir D, Fong Caroline L, Tzung Brian S, Law Meng, Nayak Krishna S. Clinical image quality assessment of accelerated magnetic resonance neuroimaging using compressed sensing. *Investigative radiology.* 2013;48:638–45.

[45] Oz Gülin, Alger Jeffry R, Barker Peter B, et al. Clinical proton MR spectroscopy in central nervous system disorders. *Radiology.* 2014.

[46] Ciccarelli Olga, Barkhof Frederik, Bodini Benedetta, et al. Pathogenesis of multiple sclerosis: Insights from molecular and metabolic imaging *The Lancet Neurology.* 2014;13:807 - 822.

[47] Bustillo Juan R.. Use of proton magnetic resonance spectroscopy in the treatment of psychiatric disorders: a critical update. *Dialogues in clinical neuroscience.* 2013;15:329–37.

[48] Ogg R J, Kingsley P B, Taylor J S. WET, a T1- and B1-insensitive water-suppression method for in vivo localized 1H NMR spectroscopy. *Journal of Magnetic RSesonance. Series B.* 1994;104:1–10.

[49] Träber Frank, Block Wolfgang, Lamerichs Rolf, Gieseke Jürgen, Schild Hans H.. 1H metabolite relaxation times at 3.0 tesla: Measurements of T1 and T2 values in normal brain and determination of regional differences in transverse relaxation *J Magn Reson Imaging.* 2004;19:537–545.

[50] Barkhuijsen H., Beer R., Ormondt D.. Improved algorithm for noniterative time-domain model fitting to exponentially damped magnetic resonance signals *Journal of Magnetic Resonance (1969).* 1987;73:553–557.

[51] Knoll Florian, Bredies Kristian, Pock Thomas, Stollberger Rudolf. Second order total generalized variation (TGV) for MRI *Magnetic Resonance in Medicine.* 2011;65:480–491.

[52] Kasten J, Lazeyras F, Van De Ville D. Data-Driven MRSI Spectral Localization Via Low-Rank Component Analysis *Medical Imaging, IEEE Transactions on.* 2013;32:1853–1863.

[53] Uecker Martin, Lai Peng, Murphy Mark J., et al. ESPIRiTâan eigenvalue approach to autocalibrating parallel MRI: Where SENSE meets GRAPPA *Magnetic Resonance in Medicine.* 2014;71:990–1001.

[54] Gruber Marvin H. J., Hayes Monson H.. Statistical Digital Signal Processing and Modeling *Technometrics.* 1997;39:335.

[55] Otazo Ricardo, Kim Daniel, Axel Leon, Sodickson Daniel K.. Combination of compressed sensing and parallel imaging for highly accelerated first-pass cardiac perfusion MRI *Magnetic Resonance in Medicine.* 2010;64:767–776.

[56] Nassirpour Sahar, Chang Paul, Henning Anke. High and ultra-high resolution metabolite mapping of the human brain using 1H FID MRSI at 9.4T *NeuroImage.* 2018;168:211 - 221.

[57] Provencher S W. Estimation of metabolite concentrations from localized in vivo proton NMR spectra. *Magnetic Resonance in Medicine.* 1993;30:672–9.

[58] Smith S.a., Levante T.O., Meier B.H., Ernst R.R.. Computer Simulations in Magnetic Resonance. An Object-Oriented Programming Approach *Journal of Magnetic Resonance, Series A.* 1994;106:75–105.

[59] Provencher Stephen W.. LCModel Website

[60] Maldjian Joseph A., Laurienti Paul J., Kraft Robert A., Burdette Jonathan H.. An automated method for neuroanatomic and cytoarchitectonic atlas-based interrogation of fMRI data sets *NeuroImage.* 2003.

[61] Fischl Bruce, Salat David H., Busa Evelina, et al. Whole Brain Segmentation *Neuron.* 2002;33:341–355.

[62] Schuff Norbert, Ezekiel Frank, Gamst Anthony C., et al. Region and tissue differences of metabolites in normally aged brain using multislice 1H magnetic resonance spectroscopic imaging *Magnetic Resonance in Medicine.* 2001;45:899–907.

[63] Pouwels Petra J.W., Brockmann Knut, Kruse Bernd, et al. Regional age dependence of human brain metabolites from infancy to adulthood as detected by quantitative localized proton MRS *Pediatric Research.* 1999;46:474–485.

[64] Natt Oliver, Bezkorovaynyy Vitaliy, Michaelis Thomas, Frahm Jens. Use of phased array coils for a determination of absolute metabolite concentrations *Magnetic Resonance in Medicine.* 2005;53:3–8.

[65] Maudsley A.A., Domenig C., Govind V., et al. Mapping of brain metabolite distributions by volumetric proton MR spectroscopic imaging (MRSI) *Magnetic Resonance in Medicine.* 2009;61:548–559.

[66] Goryawala Mohammed Z., Sheriff Sulaiman, Maudsley Andrew A.. Regional distributions of brain glutamate and glutamine in normal subjects *NMR in Biomedicine.* 2016;29:1108–1116.

[67] Maghsudi Helen, Schmitz Birte, Maudsley Andrew A., et al. Regional Metabolite Concentrations in Aging Human Brain: Comparison of Short-TE Whole Brain MR Spectroscopic Imaging and Single Voxel Spectroscopy at 3T *Clinical Neuroradiology.* 2020;30:251–261.

[68] Engl Heinz W., Grever Wilhelm. Using the L–curve for determining optimal regularization parameters *Numerische Mathematik.* 1994;69:25–31.

[69] Kumaragamage Chathura, De Feyter Henk M., Brown Peter, McIntyre Scott, Nixon Terence W., Graaf Robin A.. Robust outer volume suppression utilizing elliptical pulsed second order fields (ECLIPSE) for human brain proton MRSI *Magnetic Resonance in Medicine.* 2020.

[70] Mlynárik Vladimír, Gruber Stephan, Moser Ewald. Proton T 1 and T 2 relaxation times of human brain metabolites at 3 Tesla *NMR in Biomedicine.* 2001;14:325–331.

[71] Liu Songtao, Fleysher Roman, Fleysher Lazar, et al. Brain metabolites B 1 -corrected proton T 1 mapping in the rhesus macaque at 3 T *Magnetic Resonance in Medicine.* 2010;63:865–871.

[72] Veenith Tonny V, Mada Marius, Carter Eleanor, et al. Comparison of inter subject variability and reproducibility of whole brain proton spectroscopy *PLoS One.* 2014;9:e115304.

[73] Emir Uzay E., Sood Jaiyta, Chiew Mark, Thomas Micheal Albert, Lane Sean P.. High-resolution metabolic mapping of the cerebellum using 2D zoom magnetic resonance spectroscopic imaging *Magnetic Resonance in Medicine.* 2021;85:2349–2358.

[74] Landheer Karl, Schulte Rolf F., Treacy Michael S., Swanberg Kelley M., Juchem Christoph. Theoretical description of modern 1 H in Vivo magnetic resonance spectroscopic pulse sequences *Journal of Magnetic Resonance Imaging.* 2019:jmri.26846.

[75] Steel Adam, Chiew Mark, Jezzard Peter, et al. Metabolite-cycled density-weighted concentric rings k-space trajectory (DW-CRT) enables high-resolution 1 H magnetic resonance spectroscopic imaging at 3-Tesla *Scientific Reports.* 2018;8:7792.